Electrostatic Effects on Inertial Particle Transport in Bifurcated Tubes

Fong Yew Leong
MEBCS Program, Singapore-MIT Alliance, Singapore 117576
Dept. of Chemical and Biomolecular Engineering, National University of Singapore, Singapore 117576

Kenneth A. Smith
MEBCS Program, Singapore-MIT Alliance, Singapore 117576
Dept. of Chemical Engineering, Massachusetts Institute of Technology, Cambridge, MA 02139

Chi-Hwa Wang
MEBCS Program, Singapore-MIT Alliance, Singapore 117576
Dept. of Chemical and Biomolecular Engineering, National University of Singapore, Singapore 117576

Shuji Matsusaka
Dept. of Chemical Engineering, Kyoto University, Kyoto 615-8510, Japan

Jinsong Hua
Institute of High Performance Computing, 1 Fusionopolis Way, #16-16 Connexis, Singapore 138632

DOI 10.1002/aic.11751

Most aerosols found naturally in the ambient environment or those dispersed from artificial devices such as dry powder inhalers, are electrically charged. It is known that a strong electrostatic charge on aerosols can result in transport behavior dramatically different from that of uncharged aerosols, even in the absence of an external electric field. In the present work, we study pneumatic transport of corona-charged particles in bifurcated tubes. This is accomplished by tracking the motion of discrete particles numerically under the influence of drag, gravitational, and electrostatic forces. The model aerosol is fly ash powder, whose size and charge distributions have been determined experimentally. The electrical mobility of the charged particle cloud is modeled through coulombic interactions between discrete point charges. For the case of polydispersed particles electrically charged across a distribution, the deposition efficiency was found to be greater than what is indicated by the mean charge and size. In particular, use of negatively charged fly ash powder of mean size of 2 μm and mean charge of −1.5 C/kg led to significant increase in deposition efficiency (∼29%) compared with uncharged fly ash powder of the same size distribution (∼8%). Analysis of particle residence times suggests significant interaction between electrical and drag

---

Correspondence concerning this article should be addressed to C.-H. Wang at chewch@nus.edu.sg

forces. These findings could have implications for pneumatic powder conveying or pulmonary drug delivery applications. © 2009 American Institute of Chemical Engineers *AIChE J*, 55: 1390–1401, 2009

Keywords: aerosols, particulate flows, computational fluid dynamics (CFD), multiphase flow, particle technology

Introduction

The deposition of fine particles on surfaces has practical applications in technological[1] and medical fields.[2] These include dust collection, dry powder coating, and control of aerosol contamination of microdevices. In particular, the transport and deposition of aerosols in the tracheobronchial airways have received considerable attention. Of special interest are aerosols in the micron range, since the deposition of smaller submicron aerosols depends strongly on diffusive effects[3] and tends to be less strongly affected by the complicated flows in the bifurcated tube geometries found in the respiratory airways.[4]

There have been a number of numerical simulations of inertial particle transport and deposition in bifurcations, mostly in the form of Lagrangian particle tracking. The motion of inertial particles in a fluid is typically handled by solving the Basset–Boussinesq–Oseen (BBO) equation for the drag and gravitational forces.[5] In that way, Balásházy and Hofmann have investigated the deposition of particles in a single bifurcation for both the inspiratory and expiratory cases by using finite difference methods.[6,7] Their numerical model was later extended to incorporate the effects of asymmetry in airway branching and flow division,[8] as well as the orientation of the gravity vector.[9] The same model has been validated by a comparison with experimentally obtained deposition efficiency (DE) data provided by Kim and Iglesias.[10] In a separate study, Lee et al.[11] performed numerical simulations for a three-dimensional double bifurcation model instead of a single bifurcation model, in consideration of the fact that the air flow in the lungs is almost never fully developed. Comer et al.[12] have also conducted a numerical study on a similar three-dimensional double bifurcation model by using a finite volume method (CFX) for the fluid phase along with more physiologically representative airflow rates and a geometry corresponding to G3-5 of Weibel's model. This was soon extended to include the effects of upstream curvature in the parent tube[13] and a triple bifurcation model,[14] at the same time incorporating transient effects due to breathing patterns. Moskal and Gradoń[15] modeled both submicron and micron particulate deposition on G1-3 including turbulence effects. van Ertbruggen et al.[16] worked on a multibifurcation geometry that was digitally modeled on the basis of bronchoscopic tomography images. The Reynolds-averaged Navier–Stokes equations were solved by a finite volume method for flows in the laminar-turbulent transition regime; even though the authors did concur that the flow in the lungs is mostly laminar.

Some of the more recent studies of particle transport in the respiratory tract feature other uncommon aspects. Yang et al.[17] examined different cases of obstructed respiratory flows, which provided an indication to submicron aerosol transport relevant to specific pulmonary diseases. Longest and Xi[18] investigated the effects of particle inertia on submicron aerosol deposition in the respiratory tract. Longest and Vinchurkar[19] related CFD predictions of respiratory aerosol deposition to upstream transition and turbulence; and in a separate study, examined the effects of mesh types on the grid convergence of such studies.[20] Instead of spherical particles, Balásházy et al.[21] focused on the simulation of fiber deposition in bronchial airways.

Compared with drag and gravitational forces, electrostatic effects on charged inertial particle transport in the lungs are much less understood. Aerosol inhalation studies of charged aerosols have been conducted on human and animal subjects.[22–24] Related theoretical studies of this subject have mainly focused on charged submicron particles where the continuum approach could be applied in the context of a cylindrical geometry.[25–28]

This approach has been extended to take into account the increase in total cross-sectional area of successive generations (popularly referred to as ''the trumpet model'').[29] Other investigators working on inertial charged particles such as Rambaud et al.[30] included electrostatic force in the analysis of charged inertial particle transport in a horizontal channel, under the assumption of a continuous electrostatic field, which may not be valid in dilute solid-gas systems.

In this article, we investigate the effects of electrostatic charge on the transport and deposition of polydisperse inertial particles in the context of a single bifurcation model. Both numerical and experimental methods have been employed in the analysis. Fly ash powder has been selected as the model aerosol, since it has been used in prior electrification studies.[31]

Experiment

Determination of particle charge distribution

The objective of the experimental study is to provide a physical basis for comparison of the deposition of charged particles with the results of the numerical simulation. For consistency of electrostatic charging, corona charging is preferable over triboelectrification.[32] The experimental apparatus used for corona charging and charge measurement is as shown in Figure 1a. The powder used in the experiments was fly ash, with a density of 2300 kg/m^3 and mean count diameter (number average) of $\sim$2 μm. Before each experiment, the fly ash powder was dried for 24 h in an oven for moisture removal. During operation, the powder was fed continuously by a table feeder (Sankyo Piotech, MFOV-1) which had been modified, so that the powder was directly carried by air into a small suction nozzle. The solid-gas loading was constant at $\sim$0.02 g/L. The particles were dispersed through an ejector (Nihon Pisco, VRL50-080108) powered by a compressed air line. The average air flow rate was 50 L/min and the relative humidity was between 10 and 20% after the inlet gas supply was forced through a packed bed of silica gel beads. The dispersed particles then traveled

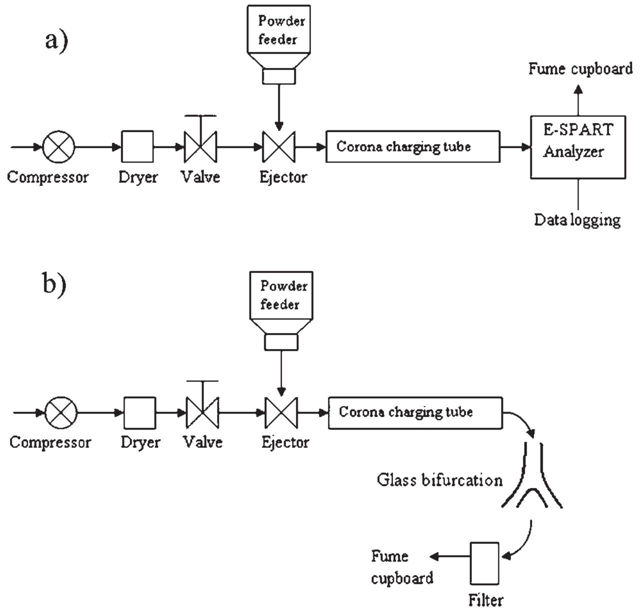

Figure 1. Schematic of apparatus used in the characterization of fly-ash powder.

(a) Determination of corona-charging efficiency using E-SPART; (b) Determination of size distribution of deposited particles in glass bifurcation model using SEM.

through a corona charging tube which consisted of a 300-mm long stainless steel tube (20 mm ID) and a 250-mm long tungsten wire of diameter 0.2 mm held taut along the axial centerline of the tube. The wire was insulated from the grounded conducting tube, but the ends of the wire were connected to a high voltage DC power supply. The limiting voltage for the formation of a corona was approximately +/−7 kV for this charger. Above the limiting voltage, current flows between the tungsten wire and the grounded tube through the migration of either positive or negative ions, depending on the polarity of the wire. Particles traveling through the corona tube are charged by the bombardment and attachment of the ions. The particle charge and the diameter distributions are measured using the electrical single particle aerodynamic relaxation time or E-SPART analyzer (Hosokawa Micron). This system was first developed by Mazumder et al.[33] and the measurements are based on the dynamics of the particle under acoustical and electrical fields. Particles are sampled from a holding chamber for charge measurement and ~5000 particle counts are registered for each run, which takes about 5 min. The particles in the chamber were continuously removed through a tube leading to a fume cupboard.

The particle charge distribution of the fly ash powder was measured by E-SPART for various magnitudes and polarities of corona current. The results are shown in Figure 2. The negative corona produces a more stable and effective charging effect than the positive corona.[32] It was also observed that even at high corona currents, a fraction of the particles is of the opposite polarity from that of the corona charger.

Determination of particle size distribution

Figure 1b shows a similar setup configuration as Figure 1a, except that the E-SPART analyzer was replaced by a model glass bifurcation connected to the corona charger by an insulated curved rubber tubing. The mother tube (MT) is 100 mm long with inner diameter of 30 mm, and it bifurcates symmetrically to two daughter tubes (DT) with a length of 90 mm and inner diameter of 20 mm. The bifurcation angle is 90°. The DT are rejoined by rubber tubes to a single outlet, which is connected to a filter canister before leading to the fume cupboard. Otherwise, the experimental protocol is the same as in the previous case.

The size distribution of fly ash powder can be determined by inspection. Particles are first sampled randomly using a small spatula and tipped onto short sections of adhesive tapes. These tapes are mounted on studs and are examined under the scanning electron microscope (SEM, model JSM-5610). Different regions on the SEM studs are inspected randomly with magnification ranging from 1000 to 5000 times. Within each region under analysis, the particle sizes are measured using a software known as Smile View (v2.0 JEOL), which had been calibrated using a target of known dimensions. The sampled particles within the field of view are then analyzed for sizes.

Before the start of the experiment, fly ash particles were sampled from the hopper feed. The size distribution was then measured and recorded in the form of a probability density function as shown in Figure 3. This result has been verified by comparing to aerodynamic size measurements made using a cascade impactor. This is used as a model input parameter in the subsequent numerical study. The fly ash particles are observed to be highly spherical with a fairly narrow size range from 1 to 10 μm. Incidentally, this size range is close to that of the standard pharmaceutical aerosols with diameters varying from 1 to 7 μm.[16]

At the conclusion of each experimental run, which lasted between 5 and 10 min, the compressed air supply, powder feed, and corona charging were disabled. The glass bifurcation was carefully removed from the connecting tubes. The deposited powder was carefully scrapped off the wall using a small spatula and then tipped onto the adhesive tape. The adhesive tape was mounted onto a metallic stud for use in SEM. The adhesive tape was not used to sample particles

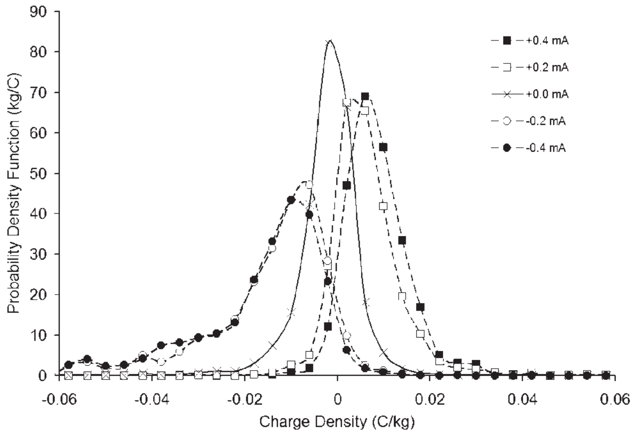

Figure 2. Charge density on fly-ash particles after corona-charging as measured using E-SPART.

Legend indicates the time-averaged magnitude of corona current applied (in mA).

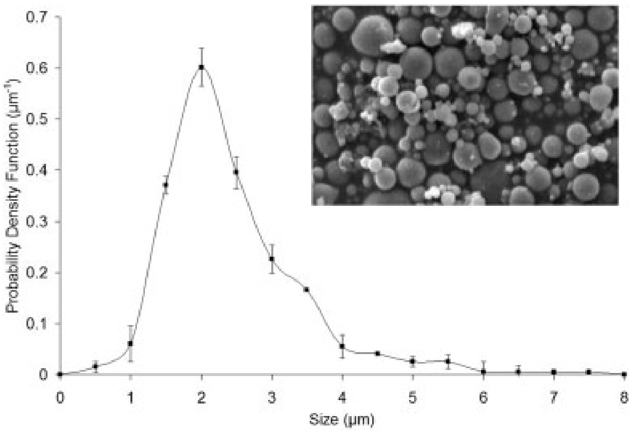

Figure 3. Size distribution of fly-ash particles obtained by inspection using Smile View (v2.0).

Inset: Scanning electron micrograph (SEM) of fly-ash particles at magnifications of ×3000.

through direct contact and adhesion because the sampled distribution would then be dependent on the adhesions strength and particle size. It is noted that some particles will be retained on the spatula after tipping but it is assumed that this constitutes an insignificant amount compared to the sample on the adhesive tape. Size distributions of the deposited fly ash powder are once more measured and compared with the original fly ash, as shown subsequently in Figure 9.

Particle Tracking Simulation

Fluid phase

The fluid phase momentum equations are solved independently of the particulate phase. The bifurcated tube geometry is a symmetrical three-dimensional model with a bifurcation half-angle of 45°. This geometry is formed simply by connecting two cylindrical daughter tubes (DT) to a single cylindrical mother tube (MT). The characteristic length-scale of choice is the radius of the parent tube, denoted by a; and the length to radius ratios for MT and DT are $L/a \sim 5.7$. The geometric discontinuity between the tubes has been smoothened with the inclusion of a sphere of radius a centered at the bifurcation axis. This geometrical configuration is shown in Figure 4a. The scaling parameter used here is the characteristic Reynolds number, defined as $\mathrm{Re} \equiv Ua/\upsilon$, where U is the centerline peak velocity at the inlet of the parent tube and υ is the kinematic viscosity of the fluid. Fully developed flow at the inlet of the parent tube is assumed. The velocity components are defined as $\tilde{u} \equiv \{\bar{u}, \bar{v}, \bar{w}\} \equiv \{u/U, v/U, w/U\}$ in Cartesian coordinates, defined as $(\bar{x}, \bar{y}, \bar{z}) \equiv \{x/a, y/a, z/a\}$ with the origin centered at the center of the MT inlet cross-section. The pressure P is normalized by $\rho U^2/2$, where ρ is the density of the fluid. The momentum and continuity equations for steady incompressible air flow are

$$(\tilde{u} \cdot \nabla)\tilde{u} = -\nabla P + \mathrm{Re}^{-1}\nabla^2\tilde{u} \tag{1}$$

$$\nabla \cdot \tilde{u} = 0 \tag{2}$$

The boundary conditions used are as follows: at the inlet of MT, the specified velocity profile is parabolic with $\bar{u} \equiv 1 - (\bar{y}^2 + \bar{z}^2)$ and null cross-sectional velocity components. The null pressure condition is imposed at the outlet boundary of each DT. The no-slip condition is imposed on all the side-walls.

Numerical simulation for the fluid phase is conducted by using the finite element method provided by the commercial software FEMLAB (v3.1). The number of finite elements used is ~80,000, and mesh invariance has been verified. The near wall mesh density is substantially higher than the average to resolve the steep velocity gradients at the near-wall region. Mesh independence is established by doubling the mesh density until the maximum and average wall shear differs by 2% or less from the previous trial.[34] The meshed geometry is shown in Figure 4b. The solver type of choice is the generalized minimum residual (GMRES) iterative solver. Numerical convergence is established at a relative tolerance of 10^{-6}.

The converged solution flow field can be visualized in the form of a velocity color map as shown in Figure 4c, for a characteristic Reynolds number of 400. This solution flow field is subsequently used in the computation of the mobility of the discrete particles under the influence of the drag force. The qualitative features of fluid flow in a single bifurcation model have been discussed extensively in the literature.[35,36] For more information on fluid flow in bifurcation models, the reader is referred to the works of Balásházy and Hofmann,[6] Comer et al.,[12] Pedley[35] as well as Schroter and Sudlow.[37] The assumption of fully developed condition at the entrance boundary of the MT means that particles near the centerline have greater specific inertia than particles further away from the centerline, and thus have a greater possibility for inertial impaction on the carinal ridge. This preferential deposition is evidenced in the deposition "hot-spots" at the carinal ridge as shown by Balásházy and Hofmann.[6] As the fluid negotiates the curvature due to the bifurcation, it experiences a pressure gradient in the secondary direction and a secondary flow is set up.[35] The secondary fluid flow can result in secondary deposition of particles on the side walls of the DTs.

Particulate phase

The numerical modeling of the particulate phase tracks the motion of individual discrete particles under the influence of various forces. We assume that the number of particle aggregates is small compared to the number of discrete particles. The equation of motion for a small rigid sphere in a fluid is commonly described by the BBO equation.[38,39] However, solution of the full BBO equation is unnecessary, since most of the force terms, other than the drag and gravitational force terms, can be neglected, as shown by order-of-magnitude arguments.[12–14] First, Brownian motion has been neglected in consideration of the size of the inertial particles.[3] Second, the particles are far denser than the fluid so that terms depending on density ratios, such as pressure and buoyancy forces, can be neglected.[40] Third, the Magnus lift force can be neglected because the particles are not spinning rapidly.[13] Finally, the shear-induced lift force, having the

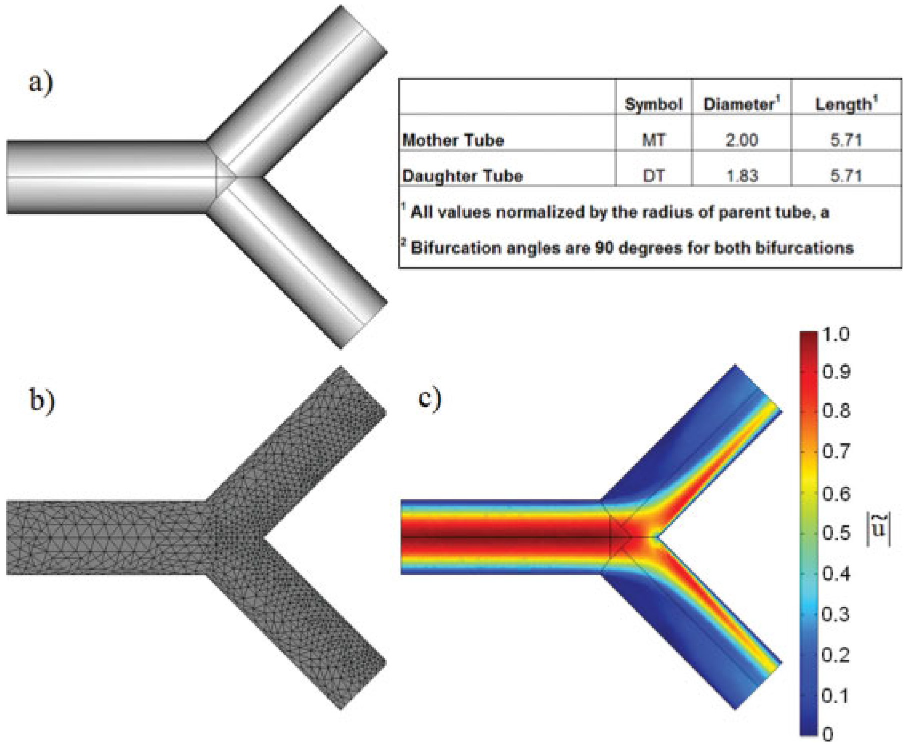

	Symbol	Diameter[1]	Length[1]
Mother Tube	MT	2.00	5.71
Daughter Tube	DT	1.83	5.71

[1] All values normalized by the radius of parent tube, a

[2] Bifurcation angles are 90 degrees for both bifurcations

Figure 4.

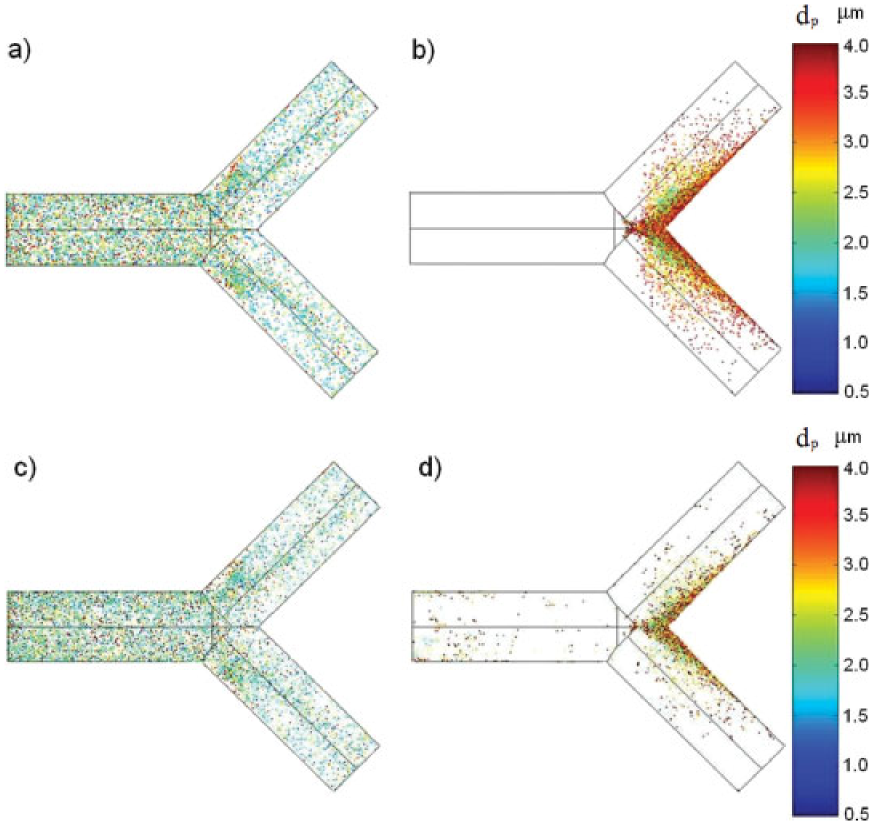

Figure 5.

form derived by Saffman for laminar flow, is found to have little effect on particle trajectories, even in turbulent flows at high Reynolds numbers.[41] There is also no clear expression for the lift force in three dimensional cases.[13]

With the above considerations in mind, the equation of motion of charged particles can be reduced to one involving only three terms, namely, the fluid drag force, gravitational force, and interparticle electrostatic interactions. The dimensional equation of motion for a single discrete ith charged sphere out of n number of charged spheres in a sea of moving fluid can be written as:

$$m_{\mathrm{p},i}\frac{\partial \bar{u}_{\mathrm{p},i}}{\partial t} = 3\pi\mu d_{\mathrm{p},i}(\bar{u}_f - \bar{u}_{\mathrm{p},i}) + m_{\mathrm{p},i}\mathrm{g} + \frac{q_{\mathrm{p},i}}{4\pi\varepsilon_0}\sum_{j\neq i}^{n}\frac{q_{\mathrm{p},j}(\bar{x}_{\mathrm{p},i} - \bar{x}_{\mathrm{p},j})}{|\bar{x}_{\mathrm{p},i} - \bar{x}_{\mathrm{p},j}|^3} \tag{3}$$

$$\frac{\partial \bar{x}_{p,i}}{\partial t} = \bar{u}_{p,i} \tag{4}$$

where $m_{\mathrm{p},i}$ is the mass of the ith particle, $\bar{u}_{\mathrm{p},i}$ and $\bar{u}_{\mathrm{f}}$ are the velocities of the ith particle and the fluid at the instantaneous particle position, respectively, t is time, μ is the dynamic viscosity of air, $\bar{g}$ is the gravitational acceleration, $q_{\mathrm{p},i}$ and $\bar{x}_{\mathrm{p},i}$ are the coulombic charge and instantaneous position of the ith particle center and ε_0 is the permittivity of free space. The subscript j refers to a particle other than i within the control volume. The Cunningham correction factor is assumed to be unity for particles within the micron size range. In addition, the bifurcation model is also assumed to be oriented vertically so that the gravitational force on the particle is parallel to the axial centerline of the MT and directed towards the carinal ridge of the bifurcation.

Implementation

Particle tracking is implemented numerically on MATLAB (7.0) for all the particles in flight by solving the equations of motion in time and space (Eqs. 3, 4). These equations have been discretized spatially by using a Taylor expansion and a central differencing scheme. The discretized forms are solved by using a finite difference method based on a simple forward time-march. The finite time-step used in this study is $\Delta t = 3\times10^{-6}s$, which is close to the particle relaxation time for a 1-micron particle in air (the smallest particle size considered in this study). The global time t is normalized by the mean fluid residence time, so that the dimensionless time can be written as $\tau \equiv t(Q/V)$, where Q is the mean volumetric flow rate and V is the control volume. By this definition, the dimensionless time step is $\Delta\tau = 0.006$.

Particles enter at the entrance boundary of the MT at each time step (immediate left edge of each subplot in Figure 4). The new particles are randomly distributed over the cross-section so that the surface density is statistically uniform. The individual particle velocities are also rendered equal to that of the fluid at the respective positions. The simulated number of particles entering the control volume per unit time-step $\dot{n}$ is 24 throughout this work. This value results in a simulated solid-gas mass loading of 0.02 g/L which corresponds to the experimental conditions using fly ash.

Discrete particles are considered *deposited* as soon as the particle center comes within a distance of one particle radius from the wall. Deposited particles are assumed to be immobilized and do not reentrain into the gas stream. This is certainly valid in the physiological airways where the walls are moist, or in deposition experiments involving liquid droplets.[42] For the present case of deposition of solid powders on hard surfaces, further justification of the particle trap condition is provided in the Appendix. Particles that exit from the outlet boundaries of the DTs are considered to have *escaped* and are no longer tracked. Particles that remain undeposited within the control volume are considered *in-flight*.

In the present study, there is no significant source of external electric field, so the only source of electrostatic influence arises from a self-induced electric field formed by a cloud of charged particles. The net electrical force is then calculated through the summation of interparticle interactions, instead of relying on an electric field that is assumed to be continuous in space and steady in time. The reason is that, for charged particles in the near-wall region, the electrical force could be significant compared to the fluid drag force. Furthermore, since particles are charged across a distribution, some particles are charged in excess of the mean value.

In the present case where the particle charge distribution is bipolar, there is a possibility of unlike point charges attracting each other indefinitely, which is computationally expensive. The solution to this problem is to cater to the possibility of collision between such particles. Consider two point charges of unlike polarities on collision. On charge transfer and neutralization, the excess charges on the particles are assumed to be redistributed between them in direct proportion to their respective surface areas (since like charges repel). However, the particles remain distinct and agglomeration does not occur.

Image charge due to the wall is assumed to be negligible compared to space charge at high charge densities.[26] Higher order induced charge effects, such as the dielectrophoretic force arising from a nonuniform electric field are also neglected, as they are several orders of magnitude smaller than the Coulombic force.

Figure 4. Top-down view of the symmetrical single 3-D bifurcation (a) and meshed model (b).

Converged velocity flow field on the center-plane is shown in (c) for Re 400. Color-bar refers to dimensionless velocity where $|\tilde{u}| \equiv \sqrt{u^2 + v^2 + w^2}/U$.

Figure 5. Particle distribution in the single bifurcation at τ = 15 and Re 400 (Top-down view).

Left column (a,c) shows particles in-flight and right column (b,d) shows deposited particles. d_p refers to particle diameter (m). (a,b): Uncharged poly-disperse particles (mean 2 μm); (c,d): Charged poly-disperse particles (mean 2 μm).

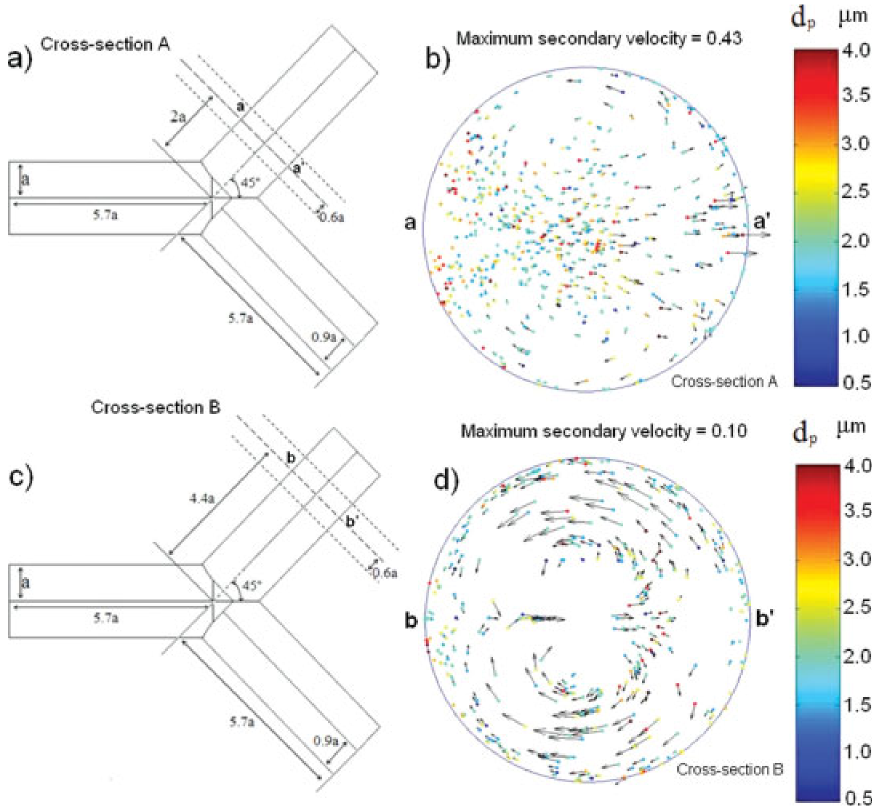

Figure 6.

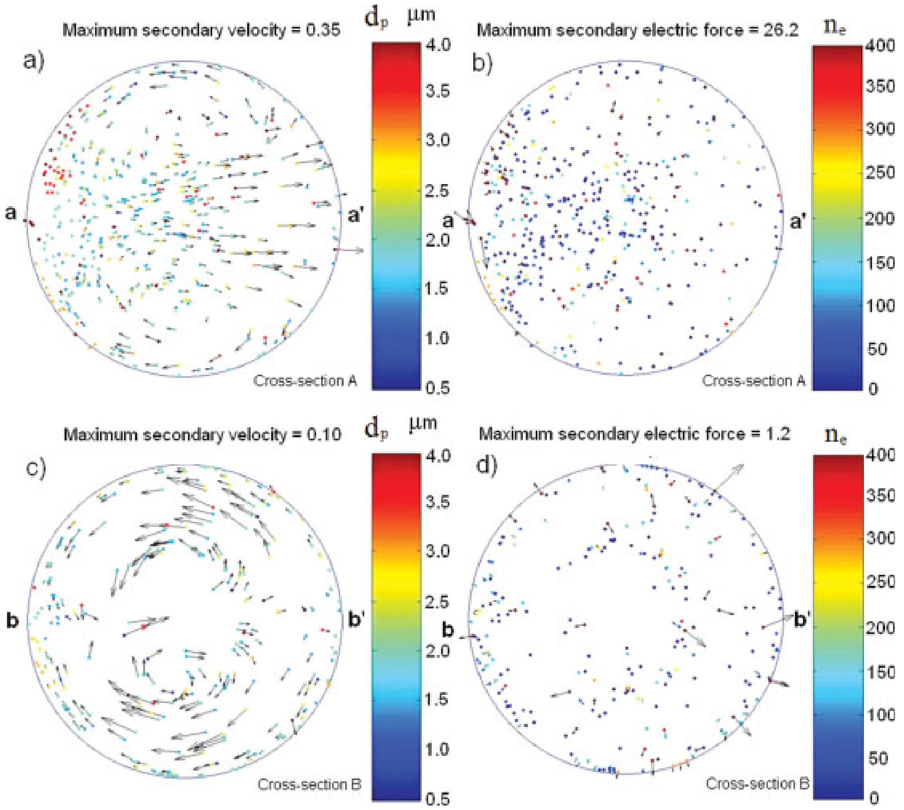

Figure 7.

Results and Discussion

Particle dynamics

The particle tracking routine has been implemented for two different cases. In the first case, we simulate motion of *uncharged* fly ash particles. We assume that the incoming particle size distribution is the same as the original particle size sample, which is measured and shown in Figure 3. For the second case, we simulate motion of *charged* fly ash particles, whose charge distribution is derived experimentally, as shown in Figure 2 (corona current of -0.2 mA).

The instantaneous spatial and size distributions of the particles at $\tau = 15$ are as shown in Figure 5. The upper row (a,b) shows the size distribution of *uncharged* particles. The bottom row (c,d) shows the size distribution of *charged* particles. In-flight particles are shown in the left column (a,c), whereas deposited particles are shown in the right column (b,d). For clarity of presentation, only particles with sizes falling within the interval $0.5\ \mu\text{m} \leq d_\text{p} \leq 4.0\ \mu\text{m}$ are distinguished by color, as indicated on the color bars shown on the right.

For the case of *uncharged* particles, it is observed that the deposited particles tend towards the red end of the spectrum and hence belong to the larger size range. There is substantial deposition of smaller particles at the carinal ridge region but far fewer small particles are found elsewhere as compared to larger particles. As a result, particles of different sizes are fractionated. A separate study using different sizes of monodisperse particles ($0.5\ \mu\text{m} \leq d_\text{p} \leq 4.0\ \mu\text{m}$) shows that the deposition profile of the polydisperse case can be derived by linear superposition of monodisperse cases. The particle tracking solution is deterministic for steady fluid flow field because the particles are assumed to be noninteracting.

In contrast to uncharged particles, *charged* particles deposit sporadically in the MT section. It might appear as though deposition of the uncharged particles at the carina is greater than the deposition of charged particles, but the opposite is true. The illusion arises from the fact that the deposition of charged particles is less spread out and is instead more focused. As the particles are interacting spatially and temporally, the deposition profile of charged particles cannot be derived from linear superposition of monodisperse cases.

As a consequence of the fluid drag, particles are strongly affected by the fluid secondary motion. Figure 6 shows the secondary trajectories of the polydisperse particles in the DT. The left column (a,c) show a top-down view of the bifurcation geometry and two cross-sections selected for examination. The distances of the cross-sections A and B from the bifurcation axis are 2.0 and 4.4, respectively, normalized by the radius of the MT. These cross-sections have a common normalized thickness of 0.6.

For the case of *uncharged* polydisperse particles, the cross-sectional particle spatial and velocity distributions are shown in the right column (b, d). The outer wall on the left is labeled as (a, b) and the inner wall on the right as (a′, b′). The particle secondary velocity vectors are self-consistent within each subplot and the magnitude of the maximum particle secondary velocity is normalized by the characteristic fluid velocity U. Larger particles are found in the recirculation zone near the outer wall compared to the mainstream flow. The particle trajectories are also observed to be significantly affected by the secondary fluid flow in the form of a pair of counter-rotating vortices.

For the case of *charged* polydisperse particles, the cross-sectional particle spatial and velocity distributions are shown in Figure 7. Particle size and velocity distributions are shown in (a, c), whereas particle charge and electrical force distributions are shown in (b, d). The vectors shown within in subplots (b, d) represent the secondary component of the electrical forces acting on the particles. The maximum electrical force is normalized by the characteristic electrical force, so that $F_\text{E} \equiv C_0 \cdot a \cdot (\bar{n}_\text{e} \cdot q_\text{e})^2 / \varepsilon_0$, where C_0 is the particle number density, a is the characteristic length, $\bar{n}_\text{e}$ is the mean number of elementary charge per particle, q_e is the elementary charge, and ε_0 is the permittivity of free space.

It is observed that the electrical force on a particle can vary by several orders of magnitude depending on the electrostatic charge on the particle itself as well as the local electric field produced by surrounding charged particles. On the basis of the maximum secondary electrical force magnitudes, a small fraction of the most highly charged particles could have an electrical force of at least the same order of magnitude as the fluid drag force, so that the influence of electrostatics should not be neglected completely. A corollary to this is that a description using a continuum electrical field would be unlikely to be accurate, because the assumed electrical field continuum would then consist of field lines radiating evenly from the center of the tube towards the walls.

Deposition efficiency

An important aspect of the particle tracking simulation is that particle deposition can be recorded and used in the validation of the numerical scheme. One common parameter used to quantify deposition is the deposition efficiency (DE).[7,12] DE is defined as the ratio of the number of

Figure 6. Particle distribution in the single planar bifurcation at cross-sections A (a,b) and B (c,d) of the left DT at τ = 15 and Re 400.

d_p refers to particle diameter (m). (a,c): Top-down view of bifurcation and cross-sections A and B. (b,d): Secondary velocity vectors of uncharged polydisperse particles found within cross-sections A and B. Maximum particle velocity magnitudes are normalized by the axial characteristic velocity.

Figure 7. Charged particle distribution in the single planar bifurcation at cross-sections A (a,b) and B (c,d) of the left DT at τ = 15 and Re 400.

d_p refers to particle diameter (*m*) and n_e refers to number of elementary charges per particle. (a,c): Secondary velocity vectors of charged poly-disperse particles. Maximum particle velocity magnitudes are normalized by the axial characteristic velocity. (b,d): Electrical force vectors of the same particles. Maximum secondary electric force magnitudes are normalized by the characteristic electric force (see text).

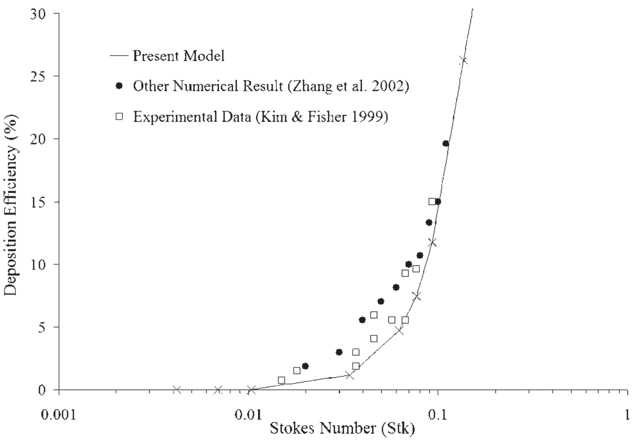

Figure 8. Comparison of the predicted uncharged particle deposition efficiency (DE) as a function of Stokes number (Stk) with other numerical[14] and experimental data.[42]

particles deposited in a given region to the total number entering the region. The calculated DE for the present numerical case studies with different monodisperse particles can then be plotted as a function of particle Stokes number (Stk). Stk is defined as Stk $\equiv \rho_p d_p^2 U/18\mu a$, where ρ_p is particle density, d_p is particle diameter, U is centerline fluid velocity, μ is fluid dynamic viscosity, and a is characteristic length. The DE profile is compared with data obtained by other investigators including a numerical study[14] and an experimental study[42] as shown in Figure 8. The agreement between the various DE profiles appears to be reasonable.

The simulated DEs of four different particle samples in the model bifurcation are shown in Table 1. The first two particle samples are monodisperse particles of 1 and 3 μm. The other two particle samples are polydisperse uncharged and charged particles. Comparison between uncharged particles of different sizes shows that larger particles tend to yield larger DEs than smaller ones. However, it is also observed that the DE of charged particles (~29%) is much greater than the uncharged case (~7.5%) for the same particle size distribution. The enhancement of DE due to electrostatic charge is remarkably large considering that the characteristic electrical force in this problem is approximately two orders of magnitude smaller than that of the characteristic drag force.

Residence time

The effects of electrostatic influence can also be observed by analyzing the mean particle residence time τ^* for various particle types (Table 1). The mean particle residence time is nondimensionalized with the mean fluid residence time, so that:

$$\tau^* = \left(\frac{n_{c.v.}}{\dot{n}_{\text{in}}}\right)\left(\frac{Q}{V}\right)\Big|_{\tau \geq \tau_{\text{eq}}} \tag{5}$$

where $\dot{n}_{\text{in}}$ is the rate of particle entering the control volume (constant), Q is the mean volumetric fluid flow at the inlet of MT and V is the control volume. The number of particles in the control volume at equilibrium, $n_{\text{c.v.}}$ is defined as $n_{\text{c.v}} = \dot{n}_{\text{in}} \cdot \tau_{\text{eq}} - \int_0^{\tau_{\text{eq}}} \left[\dot{n}_{\text{dep}}(\tau) + \dot{n}_{\text{exit}}(\tau)\right] d\tau$, where $\dot{n}_{\text{dep}}$ is the rate of particle deposition and $\dot{n}_{\text{exit}}$ is the rate of particles exiting from the outlet of the DTs. τ_{eq} is the time required for the system to attain equilibrium, at which point $\dot{n}_{\text{in}} = \dot{n}_{\text{dep}} + \dot{n}_{\text{exit}}$. It is interesting to note that the manipulated variable $\dot{n}_{\text{dep}}$ acts on the mean particle residence time τ^* only indirectly by affecting the number of particles in the control volume found at equilibrium $n_{\text{c.v.}}$.

Table 1 shows that the mean particle residence times τ^* for the 3-μm monodisperse particles are consistently lower than that for the 1-μm monodisperse particles. The first reasoning may be that particles with higher DE would spend less time on average in flight due to higher $\dot{n}_{\text{dep}}$. However, this does not explain why the polydisperse particles with a higher DE than the 1 μm monodisperse particles do not display lower average residence time. Similarly, although the DE for charged polydisperse particles is much lower than that for 3-μm monodisperse particles, the residence time is not significantly greater.

An explanation for the elevated average residence time of the polydisperse particles is that particles of moderate sizes are trapped for extended periods of time in the recirculation zone near the outer wall region. These particles loop continuously in the fluid vortex until they either deposit on the wall, or break into the fluid mainstream and escape from the outlets. Smaller particles of low inertia tend to follow the fluid streamlines well, so they are not likely to deviate from their "escape" trajectories into the recirculation zone. Although large particles are more likely to enter the recirculation zone, they are still more likely to deposit once they are brought near the wall, or escape into the mainstream.

For the case of charged particles, particles of moderate inertia are not trapped in the fluid vortex for extended period of time, since electrical forces increase their likelihood of deposition significantly once they are brought near the outer wall by the fluid. This results in early termination of the particle recirculation loop. Another contributing factor to the low particle residence time is the rapid deposition of charged particles in the MT.

Size distribution

The experimental work on fly ash provides data on particle size distributions, which can be compared against

Table 1. Deposition Efficiencies (DEs) and Particle Residence Times s* of Various Simulated Particle Input Types Under Identical Fluid Flow Conditions*

Characteristics of Particle Input	Stk	Deposition Efficiency (DE) (%)	Particle Residence Time (τ^*)
1 μm mono-disperse particles	0.03	0.93 ± 0.01	2.06 ± 0.07
3 μm mono-disperse particles	0.30	52.5 ± 1.0	1.79 ± 0.06
Poly-disperse particles (mean 2 μm)	0.12	7.57 ± 0.08	2.15 ± 0.08
Charged poly-disperse particles (mean 2 μm)	0.12	29.2 ± 0.5	1.79 ± 0.06

*For the case of charged particles refer to Figure 2 for the particle charged density.

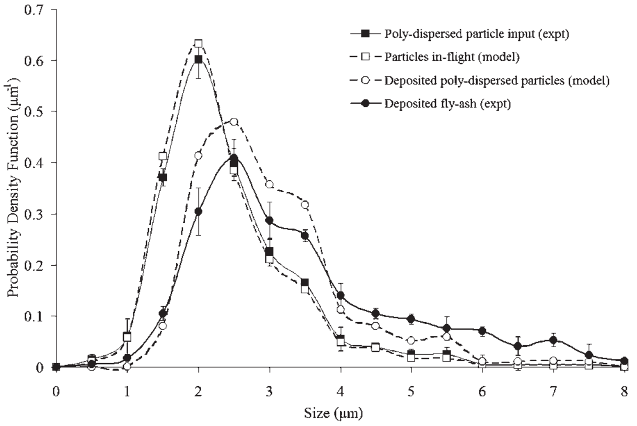

Figure 9. Size distribution of uncharged particles based on experimental (■, ●) and numerical (□, ○) data.

All values are normalized by the total number of particles sampled.

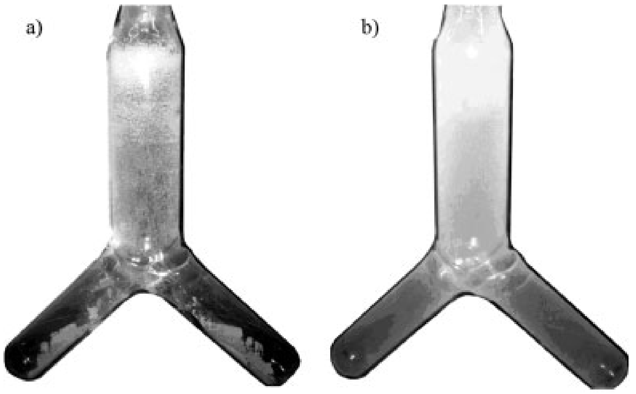

Figure 11. Observed deposition patterns of fly-ash on glass bifurcated tube after 6 min at solid mass loading of 0.02 g/L.

(a) Inertial particles impact on the carinal ridge and may slide due to gravity; (b) Charged fine particles coat the interior surfaces of the bifurcation.

predictions from numerical simulations. Figure 9 shows particle size distributions for uncharged particles at time $t = 15$. Each particle size distribution has been normalized by the total number of particles sampled instead of the total particle input. The purpose of such a renormalization is to facilitate the comparison between numerical and experimental data. The size distribution of deposited fly ash particles sampled from the experiments is found to be reasonably close to the size distribution of the deposited simulated particles. The mean size distribution of deposited particles is slightly greater than input mean size distribution due to the preferential deposition of larger particles via inertial impaction.

Figure 10 shows the particle size distributions for the case of charged polydisperse particles. The experimental particle size distribution for deposited charged fly ash particles is skewed towards the left compared to the numerical particle size distribution. For the simulated charged particles, the particle deposition in the MT shows an interesting double peaked size distribution. First, deposition of fine particles is enhanced due to electrostatic charge because the electrical forces would then compare favorably against the lower drag forces associated with smaller particles. Second, deposition of large particles is also enhanced due to electrostatic charge because the electrical force contributes to particle momentum in the direction towards the wall. For particles of moderate size, the net contribution from those mechanisms approaches a minimum. In the carinal ridge and DTs, however, the double peaked size distribution is obscured by the dominance of inertial impaction and cannot be distinguished easily.

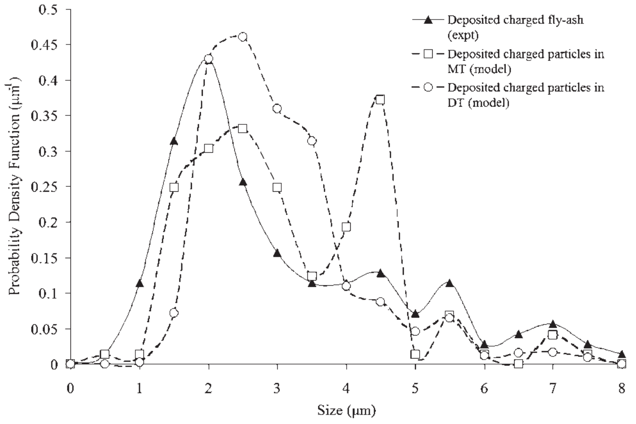

Figure 10. Size distribution of deposited charged particles based on experimental (▲) and numerical (□, ○) data.

All values are normalized by the total number of particles sampled.

The experimental results suggest that deposition of smaller charged particles creates a local electric field which limits further deposition of larger charged particles of the same polarity. Figure 11 shows experimental observations on the deposition profile of fly ash on bifurcated tubes. For the case of noncharged particles, it is numerically predicted that the bulk of the deposited particles will be located at the carinal ridge due to inertial impaction and gravitational sedimentation (see Figure 5b). However, in reality, the particles may slide due to the nonadhesive nature of the glass wall (Figure 11a). For the case of charged particles, the particles form a thin coat on the wall surface (Figure 11b). Due to the electrical insulation from the glass wall, the local electric field formed by the deposited charged particles does not leak away, so it tends to repel the larger particles that would normally impact on the carinal ridge.

Conclusions

A particle tracking routine has been employed to simulate the transport and deposition of polydisperse particles in a model bifurcation that includes a case for charged particles. It is shown that electrostatic charge on aerosols may result in transport and deposition behavior dramatically different from on uncharged ones, even if the characteristic electrostatic force appears to be negligible compared to other forces. This is particularly true for aerosols with a broad charge distribution or aerosols near the wall boundary where fluid velocities are minimal. For corona-charged fly ash particles, the overall DE is shown to be much greater than for uncharged particles. Furthermore, the presence of electrostatic charge significantly increases the DE of both the very fine and the large inertial particles in the MT, but not the particles in the moderate size range. Further work on the charged particle transport could improve our understanding of how electrostatic forces interact with other dominant forces in the context of powder dynamics.

Acknowledgements

The authors would like to acknowledge the helpful suggestions from Prof. H. Masuda and the use of E-SPART instrument from Kyoto University. The authors also thank Wei Han Ang from A*STAR Institute of Chemical Engineering Sciences (ICES) for verifying the size distribution of the fly-ash using cascade impactor. This work is kindly supported by the Singapore-MIT Alliance under the grant number C382-427-003-091 and the Science & Engineering Research Council (SERC) under the grant number R279-000-208-305.

Literature Cited

1. Kadekar V, Fang WY, Liou F. Deposition technologies for micro-manufacturing: A review. *Trans ASME.* 2004;126:787–795.
2. Dalby R, Suman J. Inhalation therapy: technological milestones in asthma treatment. *Adv Drug Deliv Rev.* 2003;55:779–791.
3. Heyder J, Gebhart J, Rudolf G, Schiller CF, Stahlhofen W. Deposition of particles in the human respiratory tract in the size range 0.0015-15 μm. *J Aerosol Sci.* 1986;17:811–825.
4. Weibel ER. *Morphometry of the Lung*. Berlin, Heidelberg, New York: Springer, 1963.
5. Morrison AR Jr. Inertial impaction in stagnation flow. *J Aerosol Sci.* 1974;5:241–250.
6. Balásházy I, Hofmann W. Particle deposition in airway bifurcations - I & II. *J Aerosol Sci.* 1993;24:745–786.
7. Balásházy I. Simulation of particle trajectories in bifurcating tubes. *J Comput Phys.* 1994;110:11–22.
8. Balásházy I, Hofmann W. Deposition of aerosols in asymmetric airway bifurcations. *J Aerosol Sci.* 1995;26:273–292.
9. Hofmann W, Balásházy I, Koblinger L. The effect of gravity on particle deposition patterns in bronchial airway bifurcations. *J Aerosol Sci.* 1995;26:1161–1168.
10. Kim CS, Iglesias AJ. Deposition of inhaled particles in bifurcating airway models: I & II. *J Aerosol Med.* 1989;2:1–27.
11. Lee JW, Goo JH, Chung MK. Characteristics of inertial deposition in a double bifurcation. *J Aerosol Sci.* 1996;27:119–138.
12. Comer CK, Kleinstreuer C, Zhang Z. Flow structures and particle deposition patterns in a double-bifurcation airway models. Part 1 & 2. *J Fluid Mech.* 2001;435:25–80.
13. Zhang Z, Kleinstreuer C, Kim CS. Effects of curved inlet tubes on airflow and particle deposition in bifurcating lung models. *J Biomech.* 2001;34:659–669.
14. Zhang Z, Kleinstreuer C, Kim CS. Cyclic μm-size particle inhalation and deposition in a triple bifurcation lung airway model. *J Aerosol Sci.* 2002;33:257–281.
15. Moskal A, Gradoń L. Temporary and spatial deposition of aerosol particles in the upper human airways during breathing cycle. *J Aerosol Sci.* 2002;33:1525–1539.
16. van Ertbruggen C, Hirsch C, Paiva M. Anatomically based three-dimensional model of airways to simulate flow and particle transport using computational fluid dynamics. *J Appl Physiol.* 2005;98:970–980.
17. Yang XL, Liu Y, Luo HY. Respiratory flow in obstructed airways. *J Biomech.* 2006;39:2743–2751.
18. Longest PW, Xi J. Computational investigation of particle inertia effects on submicron aerosol deposition in the respiratory tract. *J Aerosol Sci.* 2007;38:111–130.
19. Longest PW, Vinchurkar S. Validating CFD predictions of respiratory aerosol deposition: Effects of upstream transition and turbulence. *J Biomech.* 2007;40:305–316.
20. Longest PW, Vinchurkar S. Effects of mesh style and grid convergence on particle deposition in bifurcating airway models with comparisons to experimental data. *Med Eng Phys.* 2007;29:350–366.
21. Balásházy I, Moustafa M, Hofmann W, Szöke R, El-Hussein A, Ahmed A. Simulation of fiber deposition in bronchial airways. *Inhal Toxicol.* 2005;17:717–725.
22. Chan TL, Lippmann M, Cohen VR, Schlesinger RB. Effect of electrostatic charges on particle deposition in a hollow cast of a human larynx-tracheobronchial tree. *J Aerosol Sci.* 1978;9:463–468.
23. Jones AD, Vincent JH, Johnston AM, McMillan CH. Effects of electrostatic charge on the pulmonary deposition of mineral dust aerosols inhaled by rats. *J Aerosol Sci.* 1988;19:565–575.
24. Melandri C, Tarroni G, Prodi V, De Zaiacomo T, Formignani M, Lombardi CC. Deposition of charged particles in the human airways. *J Aerosol Sci.* 1983;14:657–669.
25. Melandri C, Prodi V, Tarroni G, Formignani M, De Zaiacomo T, Bompane GF, Maestri G. On the deposition of unipolarly charged particles in the human respiratory tract. In: Walton WH, editor. Inhaled particles IV. *Proceedings of an International Symposium organized by The British Occupational Hygiene Society, Edinburgh, 22-26 September 1975*. Vol 1. Oxford: Pergamon Press, 1977:193–201.
26. Yu CP. Precipitation of unipolarly charged particles in cylindrical and spherical vessels. *J Aerosol Sci.* 1977;8:237–241.
27. Yu CP, Chandra K. Deposition of charged particles from laminar flows in rectangular and cylindrical channels by image force. *J Aerosol Sci.* 1978;9:175–180.
28. Ingham DB. Precipitation of charged particles in human airways. *J Aerosol Sci.* 1981;12:131–135.
29. Bailey AG, Hashish AH, Williams TJ. Drug delivery by inhalation of charged particles. *J Electrostatics.* 1998;44:3–10.
30. Rambaud P, Taniere A, Oesterle B, Buchlin JM. On the behavior of charged particles in the near wall region of a channel flow. *Powder Tech.* 2002;125:199–205.
31. Matsusaka S, Umermoto H, Nishitani M, Masuda H. Electrostatic charge distribution of particles in gas-solids pipe flow. *J Electrostatics.* 2002;55:81–96.
32. Cross JA. *Electrostatics, Principles, Problems and Applications.* Bristol: Adam Hilger, 1987.
33. Mazumder MK, Ware RE, Yokoyama T, Rubin BJ, Kamp D. Measurement of particles size and electrostatic charge distributions on toners using E-SPART analyzer. *IEEE Trans Ind Appl.* 1991;27: 611–619.
34. Tadjfar M, Smith FT. Direct simulations and modeling of basic three-dimensional bifurcating tube flows. *J Fluid Mech.* 2004;519:1–32.
35. Pedley TJ. *The Fluid Mechanics of Large Blood Vessels.* Cambridge: Cambridge University Press, 1980.
36. Zhao Y, Lieber BB. Steady expiratory flow in a model symmetric bifurcation. *J Biomech Eng.* 1994;116:318–323.
37. Schroter RC, Sudlow MF. Flow patterns in models of the human bronchial airways. *Respir Physiol.* 1969;7:341–355.
38. Soo SL. *Fluid Dynamics of Multi-Phase Systems.* Waltham, MA: Blaisdell, 1967.
39. Maxey MR, Riley JJ. Equation of motion for a small rigid sphere in a non-uniform flow. *Phys Fluids.* 1983;26:883–889.
40. Clift R, Grace JR, Weber ME. *Bubbles, Drops and Particles.* New York: Academic, 1978.
41. McLaughlin JB. Aerosol particle deposition in numerically simulated channel flow. *Phys Fluids.* 1989;1:1211–1224.
42. Kim CS, Fisher DM. Deposition characteristics of aerosol particles in sequentially bifurcating airway models. *Aerosol Sci Tech.* 1999; 31:198–220.
43. Li A, Ahmadi G. Deposition of aerosols on surfaces in a turbulent channel flow. *Int J Eng Soc.* 1993;31:435–451.
44. Dahneke B. The influence of flattening on the adhesion of particles. *J Colloid Interfacial Sci.* 1972;40:1–13.

Appendix

Particle Trap Condition

The accuracy of the particle trap assumption is investigated in a separate study. Theoretically, particles are able to rebound and escape from the wall when the kinetic energy is able to overcome the attractive forces between the particle and wall surfaces. The critical approach velocity $v_{p,c}$ of the particle, above which particle rebounding occurs, is given by[43]

$$v_{p,c} = \sqrt{\frac{2E}{m_p}\left(\frac{1-S^2}{S^2}\right)} \tag{A1}$$

where S is the coefficient of restitution, m_p is the mass of the particle and E is the surface potential energy. The surface potential energy E can be expressed as

$$E = \frac{Ad_p}{12\delta_e} \tag{A2}$$

where A is the Hamaker constant (estimated to be 8.53×10^{-20} J for fly ash[44]), d_p is the diameter of the particle and δ_e is the equilibrium separation of the particle and surface, typically in the order of 4×10^{-10} m. The coefficient of restitution S is not expected to be larger than 0.1. The simulated deposition efficiency (DE) of polydispersed particles at $S = 0.3$ is only 6.3% lower than the particle trap assumption.

Further justification was provided in a physical particle entrainment study used to assess the adhesion strength between the fly ash powder and glass surface. Fly ash powder was scattered on a glass slide and examined under an optical microscope. Strong air shear was then produced on the surface of the glass slide for 1 min. Even under extremely high shear ($\sim 2.3 \times 10^{-2}$ kg/m s), one greater than that used in the main experiment ($\sim 1.8 \times 10^{-4}$ kg/m s), discrete particles were observed to persist on the slide. Only the large agglomerates were entrained. Furthermore, it was observed that a path originally free of particles remains distinct under high shear. It is inferred that discrete particles are held in position and do not translate. Therefore, the particle-wall adhesion is shown to be extremely strong and it is assumed that particles do not rebound or reentrain on wall collisions.

Manuscript received Oct. 12, 2007, and revision received Sept. 25, 2008.